Discretizations, integrable systems and computation

M J Ablowitz[1], B M Herbst[2] and C M Schober[3]

[1] Department of Applied Mathematics, University of Colorado, Boulder, CO 80309, USA
[2] Department of Applied Mathematics, University of Stellenbosch, Private Bag X1, Matieland 7602, South Africa
[3] Department of Mathematics and Statistics, Old Dominion University, Norfolk, VA 23529, USA

E-mail: cschober@lions.odu.edu

Abstract
Discretizations and associated numerical computation of solutions of certain integrable systems, such as the nonlinear Schrödinger equation (NLS) and the sine-Gordon (sG) equations with periodic boundary values can lead to instabilities, chaotic and spurious results. The chaos can be due to truncation errors or even roundoff errors and can be traced to the fact that these integrable systems are strongly unstable when the initial values are in the neighbourhood of homoclinic manifolds. By using the associated nonlinear spectral transform of the NLS equation and tracking the evolution of relevant eigenvalues one can observe and relate crossing of homoclinic manifolds to the temporal chaos in the waveforms when the initial data is even. For general initial values, even though there is no crossing of the unperturbed homoclinic manifolds, the waveforms still exhibit chaotic phenomena which can be related to the evolution of the spectrum. This paper reviews the current understanding of this intriguing phenomena and also compares the implementation of certain symplectic integrators and Runge–Kutta algorithms for the NLS and sG equations in regions of phase space proximate to the homoclinic manifolds.

PACS numbers: 02.30.Ik, 02.60.Lj, 05.45.-a

(Some figures in this article are in colour only in the electronic version)

1. Introduction

During the past 25 years an important class of nonlinear equations have been found to be integrable by means of the inverse scattering transform (IST) [2, 3]. These equations have numerous features in common, one being the existence of solitons. Solitons are stable localized waves which interact elastically with each other. Applications are diverse, ranging from

classical physics such as fluid dynamics and nonlinear optics to modern physics: particle physics, quantum field theory and relativity. There are significant applications in pure mathematics as well, for example, analysis, knot theory, algebraic geometry and group theory. While many earlier investigations emphasized the existence and stability of solitons, which remains a crucial issue in applications such as nonlinear optical communications, it was soon realized that some integrable equations of soliton theory also possess unstable structures such as homoclinic manifolds. The existence of homoclinic solutions has a profound effect on the dynamics of nearby systems and can, for example, generate chaos in perturbed nonlinear Schrödinger (NLS) and sine-Gordon (sG) systems (see e.g. [19]).

In this paper we wish to describe and review the influence these unstable structures have upon the numerical computation of the solutions and nearby discretizations. Starting with the NLS equation

$$\mathrm{i}u_t + u_{xx} + 2|u|^2 u = 0 \tag{1}$$

together with periodic boundary conditions $u(x + L, t) = u(x, t)$, we investigate the effect of numerically induced Hamiltonian perturbations in the vicinity of homoclinic manifolds. For initial values in the vicinity of 'low order' (this will be made more precise in the next section) homoclinic manifolds, it has been shown that nonintegrable perturbations, nonintegrable discretizations, may lead to chaotic solutions [5, 24, 26]. If we call h a parameter which measures the mesh size of the numerical simulation, then Mel'nikov techniques provide one with an estimate of the critical value of h necessary for the simulation to behave chaotically [25]. However, the chaos disappears rapidly as h is reduced and the calculations indicate convergence to the analytical solutions. Alternatively, one may use specially designed, integrable discretizations for the numerical simulations. In this case chaotic behaviour is not observed in the vicinity of low-order homoclinic manifolds. However, if the order of the homoclinic manifold is increased, and is sufficiently large, then small perturbations on the order of roundoff error, are enough to produce chaotic solutions even if an integrable discretization, or an infinite-order Fourier-based integrator is used, see [6, 7]. As a consequence, for some regions of phase space the 'integrable' equations are 'effectively chaotic'.

The numerically induced chaos described in the experiments above can be carefully analysed since for integrable equations such as the NLS and sG equations, the geometric structure of the phase space has been worked out in detail [16–21]. The role of homoclinic orbits in the generation of chaotic dynamics in near-integrable partial differential equation was first identified for damped-driven perturbations of the sG equation when even symmetry, $u(-x, t) = u(x, t)$, is enforced [15]. Homoclinic orbits and linear instabilities were correlated with special elements of the associated Floquet spectrum, providing a powerful tool for examining nearby systems [14]. Under the assumption of spatial evenness, the phase space is divided by the homoclinic manifolds into separate invariant regions. Due to this particular structure of phase space, the mechanism for chaotic behaviour involves frequent homoclinic crossings, similar to the well known situation for finite-dimensional systems [15].

However, if one relaxes the evenness constraint (i.e. the generic case), phase space is no longer divided into different invariant regions by the homoclinic manifolds (we provide evidence for this fact in section 2). Nevertheless, we find in numerical experiments that the waveform still displays unpredictable behaviour [8]. In this case the mechanism for the unpredictability is not associated with crossings of the unperturbed homoclinic manifold. Instead, 'transition' states develop near the homoclinic manifolds and the solution flips in an essentially random manner from left to right going waves [8]. In the even case the waveforms are standing waves; i.e. they have no left–right velocity. The homoclinic transition phenomena is a 'universal' feature associated with the modulational instability in perturbed NLS equations

and has recently been shown, experimentally and theoretically, to also be responsible for chaotic wave dynamics in water waves and nonlinear optical fibres [11, 12]. Spatiotemporal chaos is also a consequence of relaxing evenness and has been investigated in relation to effective stochastic dynamics in a damped-driven NLS system [22, 23].

In summary, depending on the order of the homoclinic manifold, which is related to the number of linearly unstable modes admitted by the initial data, we find the following. (i) The computation can be chaotic due to either truncation or roundoff effects; (ii) in the case of even initial data the numerical solutions cross the homoclinic manifold, which foliate the phase space, in a temporally irregular manner; (iii) for general initial data there need not be homoclinic crossings, but complicated, irregular evolution in time is still observed.

The sG equation

$$\phi_{tt} - \phi_{xx} + \sin \phi = 0 \tag{2}$$

is another well known integrable equation possessing homoclinic structures [18]. It is interesting that a fully discrete, completely integrable discretization can be obtained. It displays many of the characteristics of the continuous equation, including higher-order homoclinic manifolds. However, despite many attractive properties, we show that it also displays spurious numerical instabilities in the vicinity of homoclinic manifolds, see [9]. On the other hand, in an earlier study we observed that a *first* order symplectic scheme remains well behaved using the same initial values. Although higher-order symplectic schemes become unstable sooner than the first-order scheme, their behaviour is more regular than nonsymplectic schemes. Thus, one may be tempted to conclude that symplectic schemes are eminently suitable for solving the finite (but high)-dimensional Hamiltonian systems that result from spatial discretizations of the infinite-dimensional problems of soliton theory. Using the nonlinear spectrum to *define* the qualitative properties of the numerical schemes, one obtains a quantitative measure of the qualitative properties of the numerical schemes. Thus, the nonlinear spectrum allows a quantitative comparison between symplectic versus nonsymplectic schemes. In the final section we summarize the findings of the detailed comparison presented in [10]. In short, using the nonlinear spectrum as diagnostic, we find that both symplectic and nonsymplectic discretizations of the sG equation perform equally well in preserving the underlying nonlinear spectrum; moreover, the nonsymplectic discretizations are the widely available Runge–Kutta methods. Consequently this raises the question of what unique features, or advantages are gained by the use of symplectic schemes.

Our discussion commences with a study of the NLS equation.

2. The structure of the NLS phase space

The NLS equation arises as the compatibility condition between two linear operators [2]

$$\mathcal{L}^{(x)}\boldsymbol{v} = \begin{pmatrix} \partial/\partial x + \mathrm{i}\zeta & -u \\ u^* & \partial/\partial x - \mathrm{i}\zeta \end{pmatrix} \boldsymbol{v} = 0 \tag{3}$$

$$\mathcal{L}^{(t)}\boldsymbol{v} = \begin{pmatrix} \partial/\partial t - \mathrm{i}(|u|^2 - 2\zeta^2) & -\mathrm{i}u_x - 2\zeta u \\ -\mathrm{i}u_x^* + 2\zeta u^* & \partial/\partial t + \mathrm{i}(|u|^2 - 2\zeta^2) \end{pmatrix} \boldsymbol{v} = 0 \tag{4}$$

where the solution, $u(x, t)$, of the NLS equation appears as the potential in the eigenvalue problem (3). We recall that the solutions of the NLS equation are completely characterized in terms of the spectrum of $\mathcal{L}^{(x)}$ which is defined as (see e.g. [19–21])

$$\sigma(\mathcal{L}^{(x)}) := \left\{ \zeta \in \mathbb{C} | \mathcal{L}^{(x)}\boldsymbol{v} = 0, |\boldsymbol{v}| \text{ bounded } \forall x \right\}. \tag{5}$$

Since the potential $u(x, t)$ solves the NLS equation, it is of spatial period L, and the spectrum is obtained using Floquet theory. Floquet theory starts with the fundamental matrix, $M(x; u, \zeta)$ which is defined by

$$\mathcal{L}^{(x)}(u, \zeta)M = 0 \qquad M(0; u, \zeta) = \begin{pmatrix} 1 & 0 \\ 0 & 1 \end{pmatrix} \tag{6}$$

and the Floquet discriminant $\Delta(u, \zeta)$ is given by

$$\Delta(u, \zeta) := \operatorname{tr} M(L; u, \zeta). \tag{7}$$

In determining the spectrum of $\mathcal{L}^{(x)}(u, \zeta)$, condition (5) for bounded eigenfunctions yields the following condition on the discriminant

$$\sigma(\mathcal{L}^{(x)}) := \{\zeta \in \mathbb{C} | \Delta(u, \zeta) \text{ is real and } -2 \leqslant \Delta(u, \zeta) \leqslant 2\}. \tag{8}$$

In the sequel we make use of the fact that Δ is entire in $\lambda \in \mathbb{C}$ and that the spectrum is invariant under the NLS flow. The spectral quantities which we will refer to are:

(a) The simple periodic spectrum

$$\sigma^{s} = \{\zeta_j^{s} | \Delta(\zeta, u) = \pm 2, \, d\Delta/d\zeta \neq 0\} \tag{9}$$

and

(b) The double points of the periodic spectrum

$$\sigma^{d} = \{\zeta_j^{d} | \Delta(\zeta, u) = \pm 2, \, d\Delta/d\zeta = 0, \, d^2\Delta/d\zeta^2 \neq 0\}. \tag{10}$$

Together, these quantities completely determine the nonlinear mode content of the solutions of NLS and their dynamical stability. Complex double points are associated with linearized instabilities of the NLS equation and label the orbits homoclinic to the unstable solutions (for an analogous detailed discussion for the situation with the sG equation, see [18]).

For example, consider the plane wave solution, $u(x, t) = a\mathrm{e}^{2\mathrm{i}a^2t + \mathrm{i}\gamma}$, where the amplitude a is a positive real number and γ is an arbitrary phase. Since the main spectrum is time invariant we substitute $u = a$ into (3) to find $v_1(x) = A\exp(\mathrm{i}x\sqrt{a^2 + \zeta^2}) + B\exp(-\mathrm{i}x\sqrt{a^2 + \zeta^2})$, and similarly for $v_2(x)$. Thus, in this case the Floquet discriminant, Δ, is explicitly calculated as

$$\Delta = 2\cos\left(L\sqrt{a^2 + \zeta^2}\right). \tag{11}$$

According to the above definitions the spectrum consists of the real axis and a spectrum band along the imaginary axis terminating at $\pm\mathrm{i}a$. The periodic spectrum is given by

$$\zeta_n^2 = \left(\frac{n\pi}{L}\right)^2 - a^2. \tag{12}$$

Thus the band of spectrum on the imaginary axis terminates at the simple periodic spectrum $n = 0$. The remaining periodic spectrum consists of only double points (see figure 1).

It is necessary to distinguish between double points on the real axis, i.e., $0 \leqslant a^2 \leqslant (n\pi/L)^2$, and double points on the imaginary axis, i.e., $0 < (n\pi/L)^2 < a^2$. The latter are the signatures of the associated homoclinic manifold.

Analytical expressions for orbits homoclinic to the plane wave solution can be obtained (see e.g., [5]) with the simplest homoclinic orbit given by

$$u(x, t) = a\exp(2\mathrm{i}a^2 t)\frac{1 + 2\cos(px)\exp(\Omega t + 2\mathrm{i}\phi + \gamma) + A_{12}\exp(2\Omega t + 4\mathrm{i}\phi + 2\gamma)}{1 + 2\cos(px)\exp(\Omega t + \gamma) + A_{12}\exp(2\Omega t + 2\gamma)} \tag{13}$$

where

$$\Omega = \pm p\sqrt{4a^2 - p^2}$$

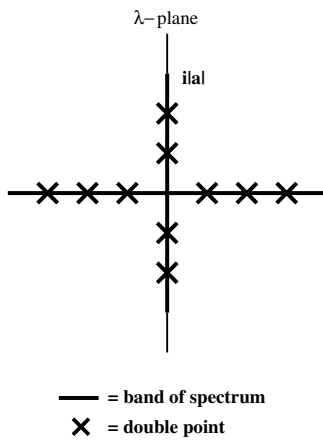$$p = 2a\sin\phi \qquad \text{and} \qquad A_{12} = \frac{1}{\cos^2\phi}.$$

Figure 1. The spectrum of the plane wave, $u = a \exp(2i|a|^2 t)$.

If $0 < p^2 < 4a^2$, this solution represents an orbit homoclinic to the plane wave solution, $u \to u_p(x, t) = a \exp(2ia^2 t)$ as $t \to -\infty$ and $u \to u_p(x, t) \exp(4i\phi)$ as $t \to \infty$. Indeed these solutions are periodic analogues of solitons and can be derived from soliton type solutions.

We note that the spectrum is invariant under the NLS flow. Since *both* the plane wave and the homoclinic solution have associated discrete spectra represented by double points on the imaginary axis, once these double points are fixed initially they remain with these values for all time. Since we are particularly interested in near-integrable behaviour, it is natural to investigate the fate of this spectral configuration under small perturbations. One of the easiest problems to consider is perturbations off a plane wave; $u_p(x, t)$ which is the asymptotic rest state of the homoclinic orbit.

Accordingly, we determine the spectral configurations of an ϵ neighbourhood of the plane wave at $t = 0$. This provides all the states that the spectrum can evolve to under small perturbations.

Let us therefore consider initial data given by

$$u = u^{(0)} + \epsilon u^{(1)} \tag{14}$$

$$= a + \epsilon \left[\exp(i\theta_1) \cos(\mu_n x) + \rho_n \exp(i\theta_2) \sin(\mu_n x) \right] \tag{15}$$

where a, ρ_n, θ_1 and θ_2 are all real, and $\mu_n = 2\pi n / L$. Initial data of this form allows us to access all the nearby states to the plane wave solution.

Since $\Delta(\zeta, u)$ and the eigenfunctions are analytic functions of u, we assume the following perturbation expansions:

$$\zeta = \zeta^{(0)} + \epsilon \zeta^{(1)} + \cdots \tag{16}$$

and

$$v = v^{(0)} + \epsilon v^{(2)} + \cdots. \tag{17}$$

This type of perturbation analysis was used to compute the splitting of double points to arbitrarily high order for even solutions [4, 7]. Here we consider the perturbation expansion for more general initial data, i.e. data which is not necessarily even. Substituting these expansions into the spatial operator, (3), and gathering terms at the various orders of ϵ, we obtain at $O(\epsilon^0)$

$$\mathcal{L}^{(x)} v^{(0)} = 0 \tag{18}$$

where

$$\mathcal{L}^{(x)} := \begin{pmatrix} 1 & 0 \\ 0 & -1 \end{pmatrix} \frac{\partial}{\partial x} - \begin{pmatrix} 0 & a \\ a & 0 \end{pmatrix} + i\zeta \begin{pmatrix} 1 & 0 \\ 0 & 1 \end{pmatrix} \tag{19}$$

and at $O(\epsilon)$

$$\mathcal{L}^{(x)} \boldsymbol{v}^{(1)} = \begin{cases} -i\zeta^{(1)} v_1^{(0)} + u^{(1)} v_2^{(0)} \\ -i\zeta^{(1)} v_2^{(0)} + u^{(1)*} v_1^{(0)}. \end{cases} \tag{20}$$

At the double points, ζ_n, the eigenspace is two-dimensional. The general solution of the leading order problem (18) is given by

$$\boldsymbol{v}^{(0)} = A^+ \phi^+ + A^- \phi^- \tag{21}$$

where $\phi^\pm$ are the eigenfunctions of the plane wave, found from (18), (19) and given by

$$\phi^\pm = \exp(\pm ikx) \begin{pmatrix} 1 \\ (i/a)(\pm k + \zeta) \end{pmatrix}$$

and $k^2 = \zeta^2 + a^2$.

Proceeding to $O(\epsilon)$, we note that the solvability condition for the system

$$\mathcal{L}\boldsymbol{v} = \boldsymbol{F} \qquad \text{with} \quad \boldsymbol{F} = \begin{pmatrix} F_1 \\ F_2 \end{pmatrix} \tag{22}$$

assuming L-periodic or anti-periodic eigenfunctions, is given by the orthogonality condition

$$\int_0^L (F_1 w_1^* + F_2 w_2^*) \, \mathrm{d}x = 0$$

for all $\boldsymbol{w}$ in the null space of the Hermitian operator, $\mathcal{L}^H$, where

$$\mathcal{L}^H = -\begin{pmatrix} 1 & 0 \\ 0 & -1 \end{pmatrix} \frac{\partial}{\partial x} - \begin{pmatrix} 0 & a \\ a & 0 \end{pmatrix} - i\zeta^* \begin{pmatrix} 1 & 0 \\ 0 & 1 \end{pmatrix}. \tag{23}$$

It follows that the null space of $\mathcal{L}^H$ is spanned by

$$\begin{pmatrix} (\phi_2^\pm)^* \\ (\phi_1^\pm)^* \end{pmatrix} \tag{24}$$

and the general solvability condition assumes the form

$$\int_0^L \left(F_1 \phi_2^\pm + F_2 \phi_1^\pm \right) \mathrm{d}x = 0. \tag{25}$$

The solvability condition applied to (20), yields the following system of equations:

$$\begin{pmatrix} -\frac{1}{2} \frac{(k+\zeta^{(0)})^2}{a^2} \alpha + \frac{1}{2}\beta & \frac{2\zeta^{(0)}}{a} \zeta^{(1)} \\ \frac{2\zeta^{(0)}}{a} \zeta^{(1)} & -\frac{1}{2} \frac{(-k+\zeta^{(0)})^2}{a^2} \beta^* + \frac{1}{2}\alpha^* \end{pmatrix} \begin{pmatrix} A^+ \\ A^- \end{pmatrix} = 0 \tag{26}$$

where

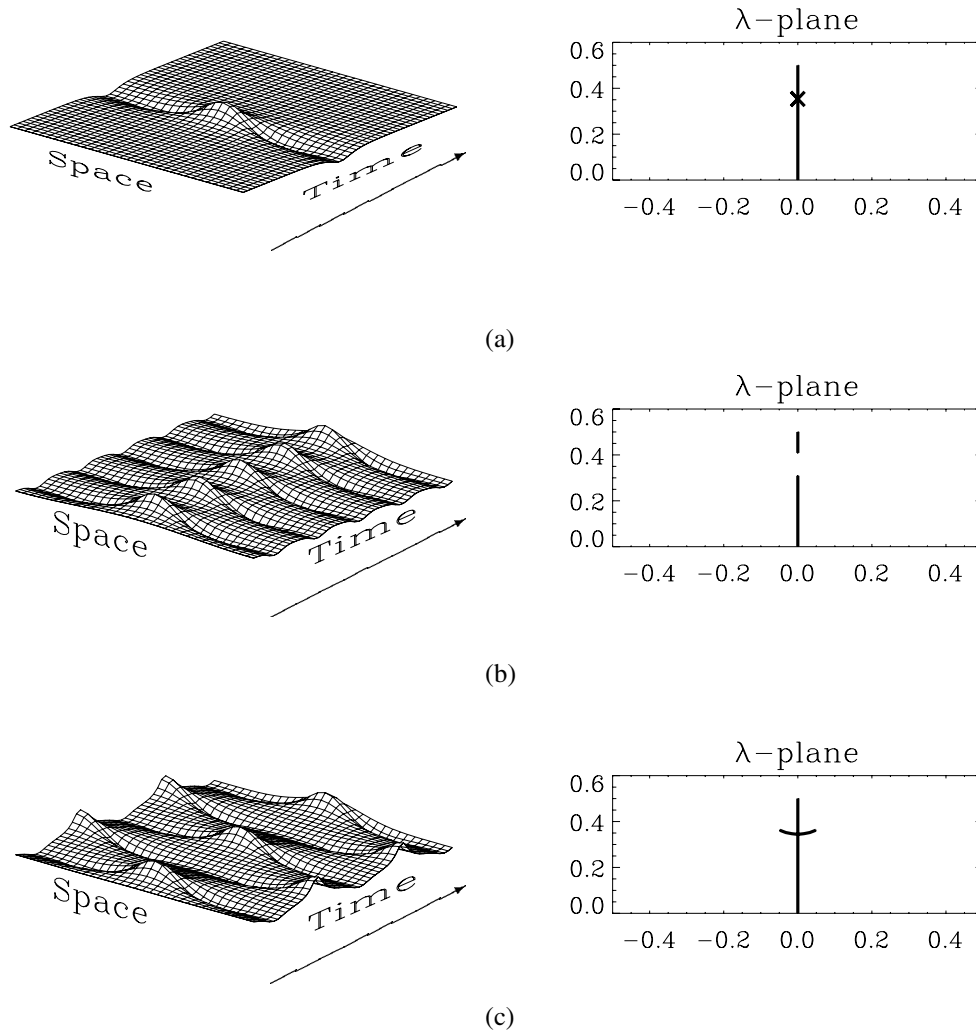$$\alpha = (\exp(i\theta_1) + i\rho_n \exp(i\theta_2)) \tag{27}$$
$$\beta = (\exp(-i\theta_1) + i\rho_n \exp(-i\theta_2)) \tag{28}$$

and $k = \frac{1}{2}\mu_n$ (for $k \neq \frac{1}{2}\mu_n$, $\alpha = \beta = 0$). This condition on k means that a specific double point is selected by the perturbation.

After some algebraic manipulation one finds in the case of imaginary double points, that nontrivial solutions, $A^\pm$, exist provided

$$(\zeta^{(1)})^2 = \begin{cases} \dfrac{a^2}{4\zeta^2} \big[\sin(\theta_1 + \psi)\sin(\psi - \theta_1) + \rho_n^2 \sin(\theta_2 + \psi)\sin(\psi - \theta_2) \\ \quad + i\rho_n \sin(\theta_2 - \theta_1)\sin(2\psi) \big] & \text{if } k = \mu_n/2 \\ 0 & \text{if } k \neq \mu_n/2 \end{cases} \tag{29}$$

where $\tan\psi = \mathrm{Im}\,(\zeta^{(0)})/k$.

(a)

(b)

(c)

Figure 2. (*a*) The surface $|u(x, t)|$ and the nonlinear spectrum with one double point for a homoclinic solution of NLS, $\zeta^{(1)} = 0$. (*b*) The surface $|u(x, t)|$ and the nonlinear spectrum with one imaginary gap for a standing wave solution of NLS, $u(x, 0) = 0.5(1 + 0.1 \cos \mu x)$. (*c*) The surface $|u(x, t)|$ and the nonlinear spectrum with one cross for a solution of NLS locked in the centre and wings, $u_0 = 0.5(1 + 0.1i \cos \mu x)$.

We consider two cases:

Symmetric case. If $\theta_1 = \theta_2$ or $\theta_1 = \theta_2 \pm \pi$ then u is symmetric and the right-hand side of (29) is real and can be either negative, zero or positive. If $\zeta^{(1)} = 0$ the double point does not split and this is then the initial value for a solution which belongs to the isospectral set of the plane wave (see figure 2(*a*)). Since the homoclinic orbit limits to the unstable plane wave as $t \to \pm\infty$, it clearly also belongs to the isospectral set of the plane wave solution. In fact, one can check directly that the initial value obtained from $\zeta^{(1)} = 0$ lies on the homoclinic orbit given by (13).

When the complex double point splits into two simple points, it can only split in one of two directions: along the imaginary axis (gap configuration, see figure 2(*b*)), or symmetrically

about the imaginary axis (cross configuration, see figure 2(*c*)). Solutions 2(*b*) and (*c*) can be thought of as 'inside' and 'outside' the homoclinic orbit, respectively. *Thus, in the symmetric case, the homoclinic orbit separates the symmetric subspace into disjoint invariant submanifolds.* Due to the analyticity of the discriminant Δ, under small perturbations it is possible to evolve from one configuration to another, while maintaining symmetry, *only* by passing through the complex double point, i.e. by crossing the homoclinic manifold.

Asymmetric case. If $\theta_1 \neq \theta_2$, $\theta_1 \neq \theta_2 \pm \pi$, and $\rho_n \neq 0$ i.e. u is asymmetric, then the right-hand side of (29) is complex. In this case, calling $\zeta^{(1,\pm)} = \pm\rho^{\frac{1}{2}}e^{i\phi/2}$, ϕ can take on any value between 0 and 2π. *Thus, in the asymmetric case, the double point can now split in any direction and the full NLS level sets are connected.* However, as we now illustrate numerically, in the one complex double point regime there are only two basic spectral configurations and the location of $\zeta^{(\pm)}$ determines the speed and direction of the travelling wave, where $\zeta^{(\pm)} \equiv \zeta^{(0)} + \epsilon\zeta^{(1,\pm)}$.

- For $0 < \phi < \pi$, ζ^+ moves into the right quadrant and ζ^- moves into the left quadrant. The resulting upper band of spectrum lies in the right quadrant and the lower band lies in the left quadrant. Figure 3(*a*) shows that the wave form is characterized by a single mode travelling to the right ('right state').
- For $\pi < \phi < 2\pi$, the situation is reversed. ζ^+ moves into the left quadrant while ζ^- moves into the right quadrant. The resulting upper band of spectrum lies in the left quadrant and the lower band lies in the right quadrant. As illustrated by figure 3(*b*), this wave form is characterized by a single mode travelling to the left ('left state').

A more detailed analysis (see [8]) shows that under asymmetric perturbations the band of spectrum on the imaginary axis breaks and the *only* two configurations that are possible are equivalent to the spectral configurations shown in figures 3(*a*), (*b*). The only situation for which the band of spectrum on the imaginary axis remains unbroken, is for the special sub-class of even solutions (allowing translations).

Under near-integrable dynamics the solution may switch between the two different configurations allowed by the asymmetric perturbations. The significance of the arguments above is that the switch may take place by passing through a nearby gap or cross state. *It is no longer necessary to pass through a double point, i.e. a homoclinic orbit*, see figure 7.

We now proceed to investigate in more detail how the structure of the NLS phase space influences numerical computations, starting with symmetric perturbations.

3. Symmetric perturbations

Consider the following second-order finite difference discretization of the NLS equation

$$i\ddot{U}_j + (U_{j-1} - 2U_j + U_{j+1})/h^2 + 2|U_j|^2 U_j = 0 \tag{30}$$

where $h = L/N$ is the grid spacing and periodic boundary conditions are enforced through $U_{j+N} = U_j$. Although this scheme does not preserve the integrability of the NLS equation, it does preserve even symmetry, i.e. if $U_j(0) = U_{-j}(0)$ then $U_j(t) = U_{-j}(t)$, $\forall t > 0$. It should also be observed that (30) can be written as a Hamiltonian system. Thus it can be considered as a model NLS system under Hamiltonian perturbations. It also arises in a variety of physical problems, for example, discrete self trapping (see e.g., [28] and references therein). In order to investigate the effect of these perturbations in the vicinity of homoclinic manifolds, we consider the following initial values:

$$u(x, 0) = a(1 + 0.1\cos(\mu x)) \tag{31}$$
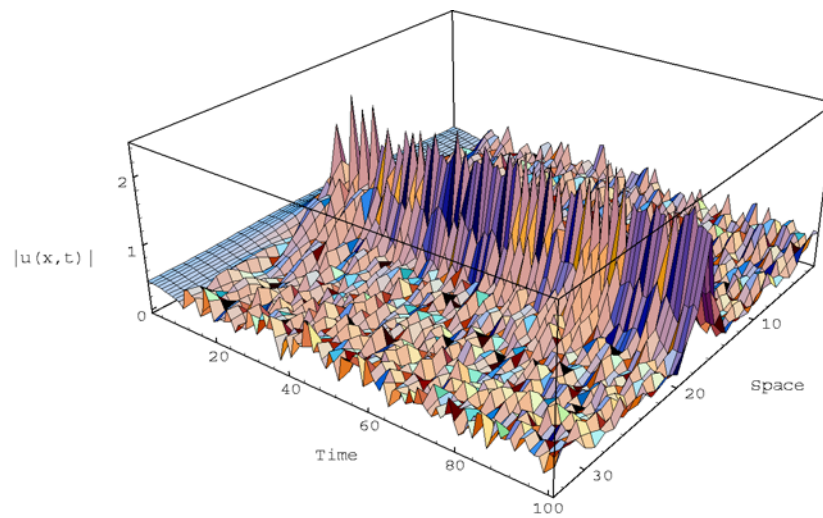
(a)

(b)
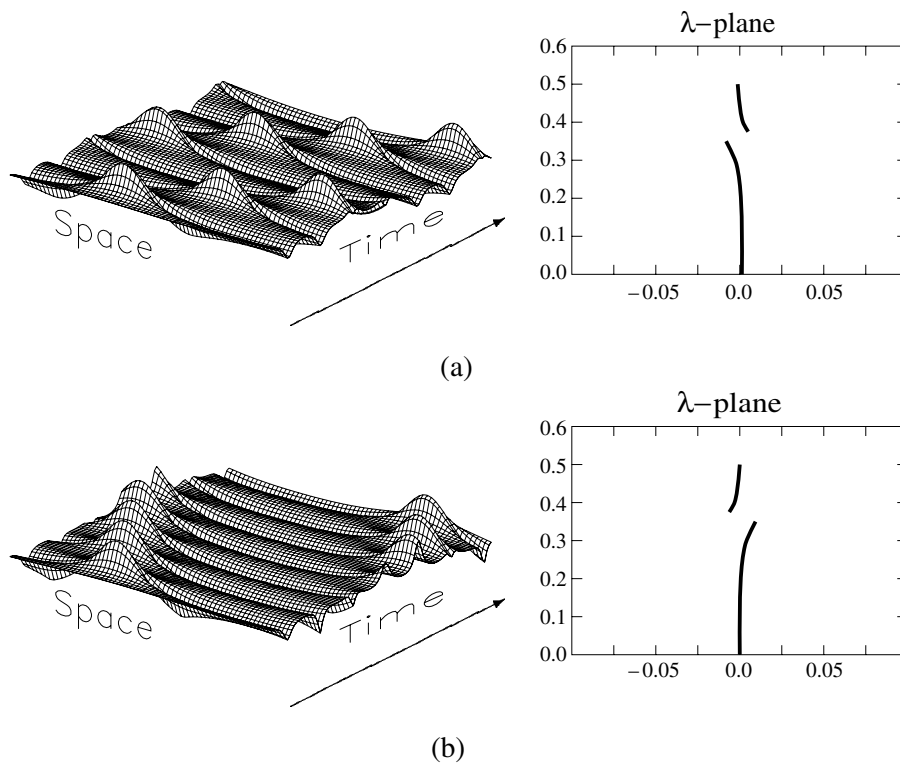
Figure 3. (*a*) 'Right' state; the surface $|u(x, t)|$ and the nonlinear spectrum for a right travelling wave solution of NLS, $u_0 = 0.5(1 + 0.05(e^{0i} \cos \mu x + e^{30i} \sin \mu x))$. (*b*) 'Left' state; the surface $|u(x, t)|$ and the nonlinear spectrum for a left travelling wave solution of NLS, $u_0 = 0.5(1 + 0.05(\exp(90i) \cos \mu x + \exp(0i) \sin \mu x))$.
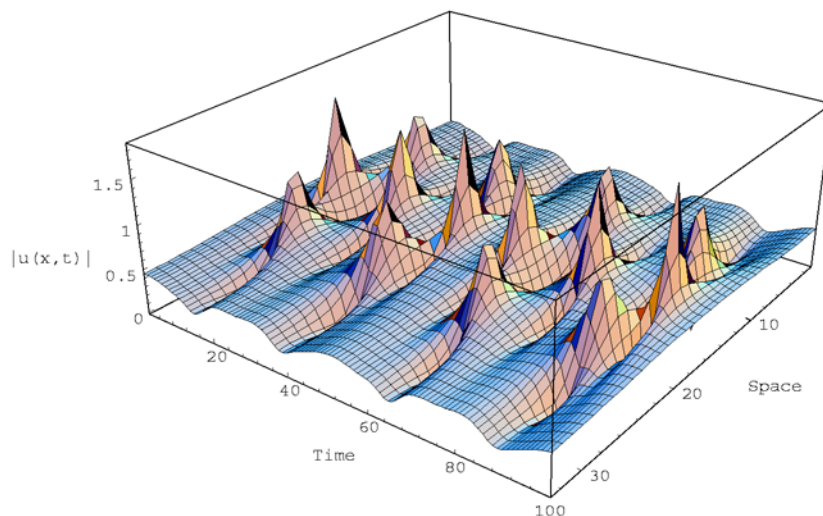
with $a = 0.5$, $L = 4\sqrt{2}\pi$ and $\mu = 2\pi/L$. A comparison with (12) reveals that these values correspond to two double points on the imaginary axis for the constant potential. The perturbation in (31) opens both double points; the first one opens a distance approximately $\mathcal{O}(0.1)$ and the second approximately $\mathcal{O}(0.01)$. Thus, the initial values are chosen close to, but not on the homoclinic manifold. For the time integration the Runge–Kutta–Merson routine, D02BBF, in the NAG library is used with the relative error specified as 10^{-10}. The results using $N = 32$ are shown in figure 4(*a*). Note the quick and complete breakdown of the spatial structure.

In order to learn more about the mechanism responsible for this breakdown, we calculate the nonlinear spectrum of the numerical solution. Recall that under small perturbations each complex double point splits into two simple points and that the manner of the splitting depends on whether the perturbation is even or not. When the double point splits for even initial data, $(\lambda_+ - \lambda_-)$ is either real or pure imaginary; i.e. the double point splits into either a 'gap' state along the imaginary axis or into a 'cross' state symmetrically about the imaginary axis. In the even experiment shown in figure 5, we monitor the evolution of the splitting distance, defined as

$$D(\lambda_+, \lambda_-) := \begin{cases} +|\lambda_+ - \lambda_-| & \text{if} \quad \text{Re}\,(\lambda_+ - \lambda_-) = 0 \\ -|\lambda_+ - \lambda_-| & \text{if} \quad \text{Im}\,(\lambda_+ - \lambda_-) = 0. \end{cases}$$

(a)

(b)

Figure 4. (*a*) Complete breakdown of the standard finite difference scheme. (*b*) The regular solution obtained from the integrable discretization. Both discretizations use $N = 32$.

Initially, the double points are split due to the perturbation of the constant potential and the nonintegrability of the numerical flow is reflected in the time evolution of the spectrum. Note in particular how the spectral configuration switches between 'cross' and 'gap' states. Since we enforce evenness in these calculations, this can only happen by moving through a double point configuration; frequent homoclinic crossings are observed.
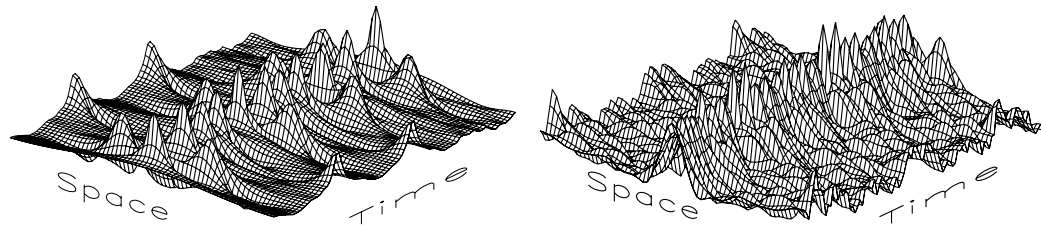
(a)
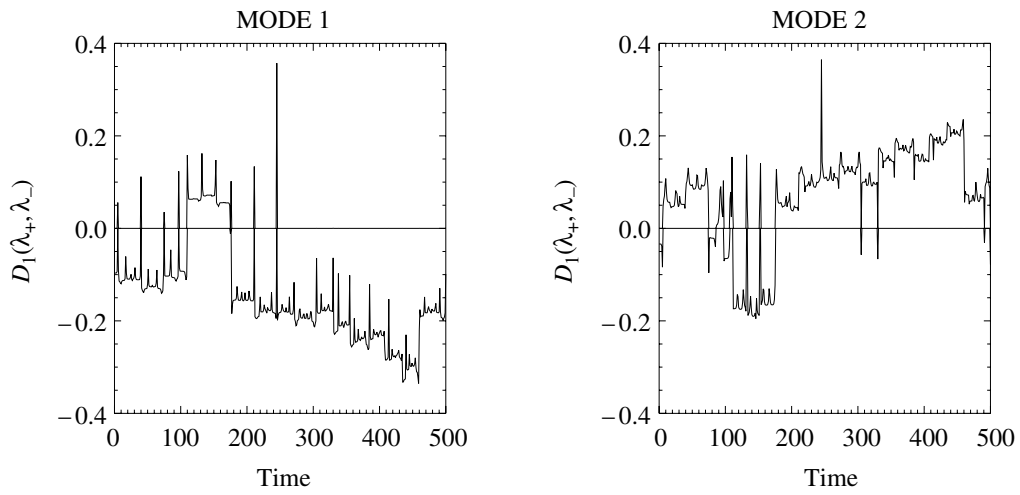
(b)
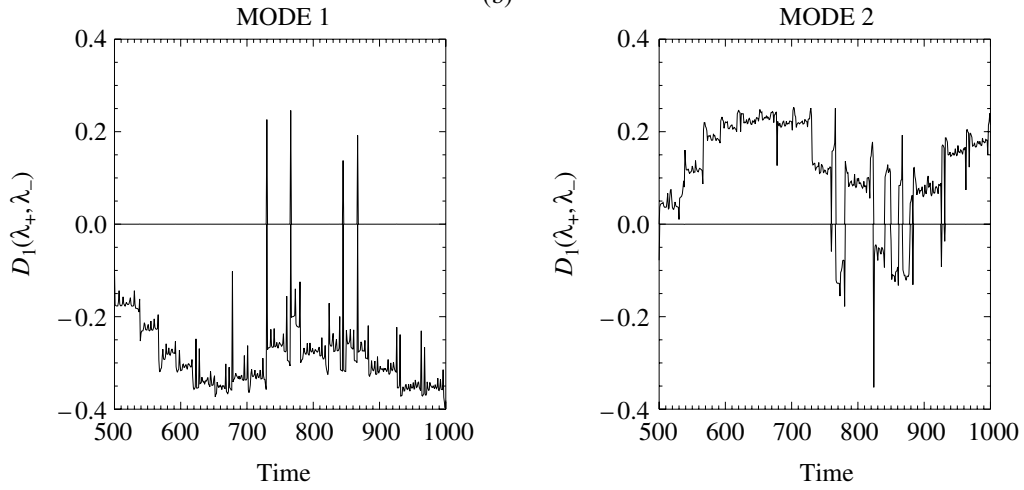
(c)

Figure 5. (*a*) Surface for even initial data $u_0 = 0.5(1 + 0.2\cos\mu x)$, $N = 64$, obtained from the standard difference scheme for $0 < t < 900$ and $900 < t < 1000$. Even symmetry is preserved. (*b*), (*c*) The evolution of $D_1(\lambda_+, \lambda_-)$ for the first and second modes for $0 < t < 500$ and $500 < t < 1000$, respectively.

The nonintegrable behaviour described above is next compared with the solutions of the integrable discretization due to Ablowitz and Ladik [1]

$$i\dot{U}_j + (U_{j-1} - 2U_j + U_{j+1})/h^2 + |U_j|^2(U_{j-1} + U_{j+1}) = 0. \tag{32}$$

Note that is also second order accurate and any differences with the nonintegrable scheme (30) appears only at $\mathcal{O}(h^4)$. Despite these seemingly innocuous differences, the numerical behaviour is very different. Using exactly the same parameter values as before, including the use of the NAG routine, the numerical solution is shown in figure 4(*b*). There is no indication of any instability (as might be expected from an integrable scheme).

Even in the case of the nonintegrable scheme, the instabilities disappear as the grid is refined. However, a more troublesome aspect of the instability becomes apparent if the initial values are chosen close to more complicated homoclinic manifolds. Accordingly, consider the integrable discretization (32) as well as the mathematically equivalent one:

$$i\dot{U}_j + (U_{j-1} - 2U_j + U_{j+1})/h^2 + |U_j|^2 U_{j-1} + |U_j|^2 U_{j+1} = 0. \tag{33}$$

Using these two schemes with $a = 5/2$, $L = 2\sqrt{2}\pi$ and $N = 512$ together with the NAG routine D02BBf, as before, the solutions are shown in figure 6(*a*). In this figure lighter shades of grey indicates larger values of the modulus. Note that the two mathematical equivalent schemes produce very different solutions! In these calculations the mathematical equivalence of the two schemes is destroyed by roundoff error which, incidentally, is also responsible for the loss of evenness in the spatial structure. Thus we find that both schemes are very sensitive to small perturbations, even on the scale of roundoff error. The explanation lies in the proximity of the homoclinic manifold.

The initial values chosen for these experiments correspond to seven complex double points of the constant potential. The perturbation added to the constant potential through the initial values (31), causes the double points to split, i.e. the initial value moves away from the homoclinic manifold. The size of the perturbation (ϵ) does not by itself tell us the 'distance' from the homoclinic manifold. The situation is more complicated. The first double point is split $\mathcal{O}(\epsilon \propto 0.1)$ as indicated by the perturbation analysis of the previous section. However, if the analysis is carried through to higher order, one finds that the second double point is split to $\mathcal{O}(\epsilon^2)$, and the nth is split to $\mathcal{O}(\epsilon^n)$, see [7]. Since we are dealing with seven double points, the initial values are, in fact extremely close to the homoclinic manifold; essentially within rounding error. Thus small perturbations are quickly amplified to become as big as the main wave. It is important to note that for a sufficiently large number of unstable modes and correspondingly high-order homoclinic manifold, it is in practice impossible to avoid proximity to the manifold. Any small perturbation, regardless of its direction, remains close to the manifold. The integrable system has indeed become effectively chaotic. In these cases the size of the perturbation even though it might be on the order of roundoff is larger or comparable to the distance to the homoclinic manifold.

4. Unpredictability without homoclinic crossings

In figure 6 symmetry was not imposed on the numerical calculations and we observed that the numerical solution lost its spatial symmetry after a reasonably short time. Recall that this loss of even symmetry is entirely due to rounding error which implies that the system is very sensitive even to the smallest perturbations. In physical situations we have even less control over small experimental errors and it is therefore unlikely that even symmetry can be preserved in practice. What is of major interest to us is that the even symmetry is closely related to the homoclinic division of the NLS phase space into separate, invariant regions. The loss of even

(a)

(b)
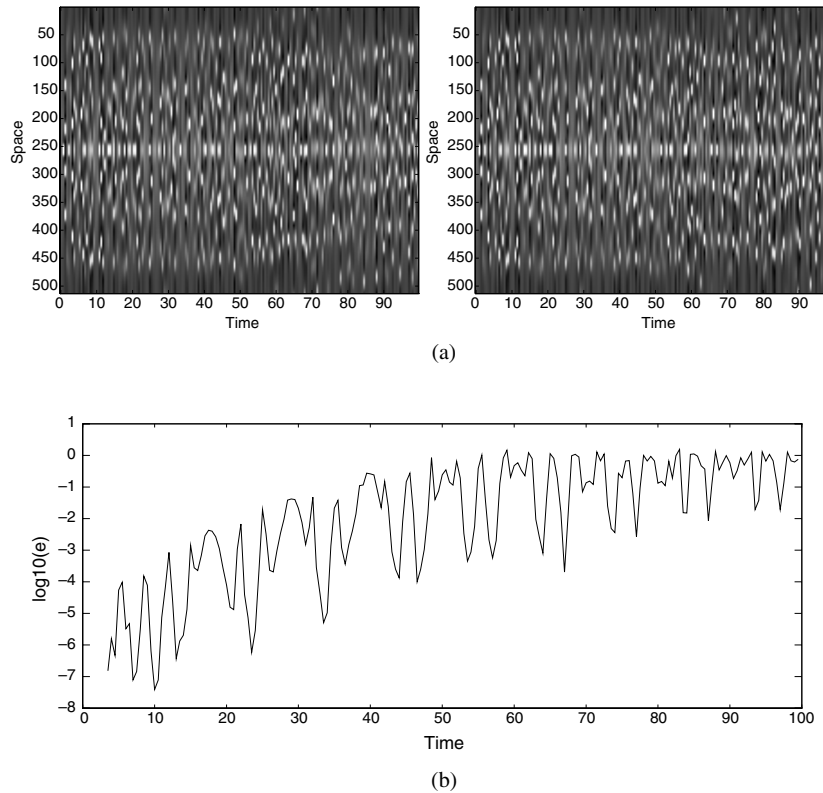
Figure 6. (*a*) The solution obtained from the two mathematically equivalent forms of the integrable discretization, (32) and (33). (*b*) The L^2 norm of the difference between the two solutions.

symmetry destroys this structure; there is no longer an 'inside' and 'outside' of the homoclinic manifold. One must therefore ask whether it is possible to observe the homoclinic manifolds in practice, or to what extent the NLS dynamics is governed by the presence of a nearby homoclinic manifold. Accordingly, we return to the nonintegrable discretization (30) together with typical initial values for, say a left travelling wave

$$u(x, 0) = 0.5(1 + 0.01(\exp(0.9i) \cos \mu x + \exp(60i) \sin \mu x)) \tag{34}$$

with $L = 2\sqrt{2}\pi$ and $\mu = 2\pi/L$. Note that this corresponds to one unstable mode. Using $N = 24$ and the adaptive Runge–Kutta–Merson routine D02BBf in the NAG library, the solution is shown in figure 7. The waveform starts out travelling to the left and as time evolves the perturbation induced by the discretization causes the waveform to flip between left and right travelling waves in a seemingly chaotic manner. During the time interval presented, the wave changes direction only twice. However, for long-time simulations a frequent random flipping in direction is observed, see [8]. Figure 7(*a*) shows the evolution of the spectrum associated with the waveform of figure 7(*b*), at three successive timeslices at the time when the waveform switches from a right to a left travelling wave. Note that the travelling wave shifts direction by evolving through a nearby cross state (associated with a stationary wave) and *not* by executing homoclinic crossings. We believe that this is truly distinctive and we emphasize that homoclinic crossings are not associated with the irregular behaviour as they were in the studies discussed in the previous section.

(a)

t = 131.5 t = 131.8 t = 132.1

(b)
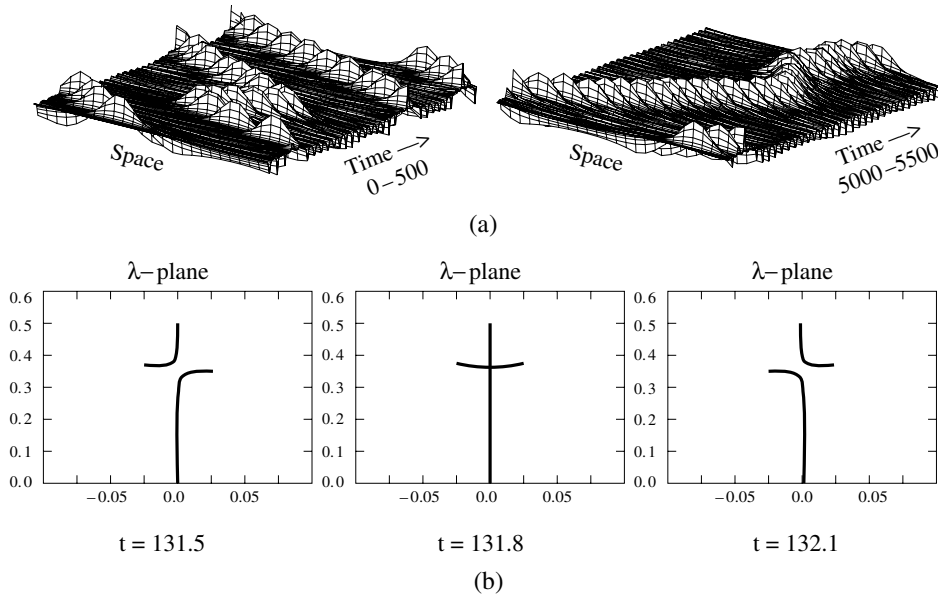
Figure 7. (*a*) Waveform obtained from $u(x, 0) = 0.5(1+0.01(\exp(0.9i)\cos\mu x + \exp(60i)\sin\mu x))$ obtained from the standard finite difference scheme for $0 < t < 500$ and $5000 < t < 5500$. The first bifurcation from a left to a right travelling wave occurs at $t = 131.8$. (*b*) The nonlinear spectrum at three timeslices showing that the transition from a 'left' ($t = 131.5$) to a 'right' ($t = 132.2$) travelling wave occurs through a 'cross' state ($t = 131.8$).

5. The sine-Gordon equation

In section 3 it was demonstrated that the integrable discretization (32) of the NLS equation is numerically superior to the nonintegrable discretization (30). Therefore, one might conclude that it is important to preserve integrability numerically, in particular if initial values are chosen in sensitive regions of phase space.

The integrable discretization (32) is continuous in time and hence its integrability is lost during the time discretization. In the experiments reported above, the accuracy of the time integrator was sufficiently high so that none of the observations are attributed to the time discretization. A particularly simple doubly discrete (space and time), integrable discretization is available for the sG equation (see [9, 13, 27])

$$(1 - \tfrac{1}{4}h^2)\tan\tfrac{1}{4}(\phi(x+h, t) + \phi(x-h, t)) = (1 + \tfrac{1}{4}h^2)\tan\tfrac{1}{4}(\phi(x, t+h) + \phi(x, t-h)). \tag{35}$$

It should be pointed out that the formalism used to derive this equation (see [9, 13]) forces the time and spatial discretization parameters to be the same, denoted by h in (35).

It is sometimes more convenient to use alternative forms of equation (35). Making use of the identity, $\tan^{-1} x = (1/2i)\ln[(1 + ix)/(1 - ix)]$, it follows after some manipulation (see [9, 13]) that (35) may be written as

$$\frac{1}{2}(\phi_m^{n+1} + \phi_m^{n-1}) = \frac{1}{2}(\phi_{m-1}^n + \phi_{m+1}^n) + i\ln\left[\frac{1 + \tfrac{1}{4}h^2\exp\tfrac{1}{2}i(\phi_{m+1}^n + \phi_{m-1}^n)}{1 + \tfrac{1}{4}h^2\exp\tfrac{1}{2}(-i)(\phi_{m+1}^n + \phi_{m-1}^n)}\right] \tag{36}$$

where $\phi_m^n := \phi(mh, nh)$. Alternatively, substituting
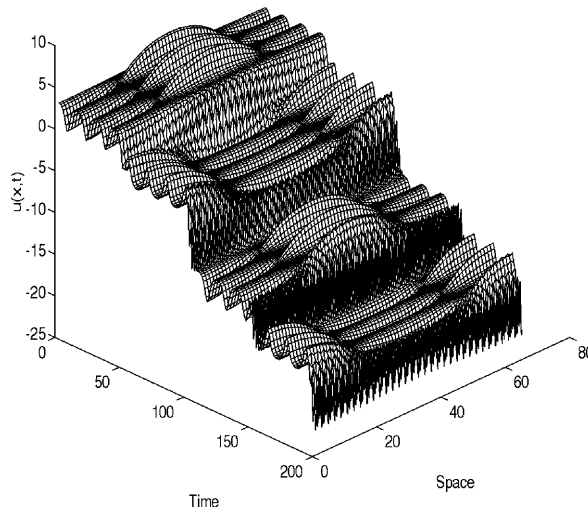
$$Q_m^n = \exp(\tfrac{1}{2}i\phi_m^n) \tag{37}$$

Figure 8. The integrable discretization of the sG equation.

into (36) we obtain

$$Q_m^{n+1} Q_m^{n-1} = \frac{Q_{m+1}^n Q_{m-1}^n + \frac{1}{4}h^2}{1 + \frac{1}{4}h^2 Q_{m+1}^n Q_{m-1}^n}. \tag{38}$$

All these different forms represent second-order accurate discretizations of the sG equation (2), when used as a numerical scheme.

It is possible to construct several special solutions of (35), see [9]. A particularly illuminating one is the homoclinic orbit given by

$$\phi(x, t) = \pi + 4 \tan^{-1}\left[\frac{b_1}{b_2} \cos(\mu x + \alpha_1) \mathrm{sech}(\gamma t + \alpha_2)\right] \tag{39}$$

where

$$(1 - \tfrac{1}{4}h^2) \cosh \gamma h = (1 + \tfrac{1}{4}h^2) \cos \mu h$$

and

$$b_2^2 \sinh^2 p_2 h = b_1^2 \sin^2 p_1 h.$$

Note that this solution has exactly the same form as a corresponding homoclinic orbit of the continuous equation, apart from a phase shift (this is a feature of many integrable discretizations; namely they have virtually the same analytic structure as their continuous analogue).

With the credentials of the integrable discretizations apparently established, let us investigate its numerical behaviour by considering the following initial values:

$$u(x, 0) = \pi + \epsilon_0 \cos(\mu x) \qquad u_t(x, 0) = 0 \tag{40}$$

with $\mu = 2\pi/L$ and $L = 2\sqrt{2}\pi$. The result of integrating (35) over 200 time units using $N = 63$, $\epsilon_0 = 0.05$ is shown in figure 8. Note the homoclinic crossings when the solution is translated through a multiple of 2π, as well as the oscillations on a grid scale.

Without going into any further details (see [9]) it suffices to say that while the behaviour shown in figure 8 is indeed a true feature of the integrable discretization; i.e. the scheme can be shown to be (35) linearly unstable and hence the complication is therefore not totally

unexpected. We also remark that there is a significant difference between whether N is even or odd. A careful study of the structure of the sG phase space reveals that the initial values (40) indeed lies on a homoclinic manifold. The homoclinic crossings as well as the oscillations of figure 8 are a consequence of the sensitivity caused by the underlying homoclinic manifold.

Of course what this means in practice is the following: even when an integrable scheme is developed, one still must analyse its stability, accuracy and ability to calculate efficiently.

6. Symplectic integrators

Numerical studies of low-dimensional canonical Hamiltonian systems have established that symplectic schemes preserve the phase space geometry very accurately over very long time periods: in fact, much better than nonsymplectic schemes [29]. However, the practicality of symplectic integrators for high-dimensional systems is less well established. To address this issue, we compare the performance of symplectic integrators and standard Runge–Kutta integrators for the NLS and sG equations [9, 10, 30, 31].

We begin by considering the integrable discrete NLS (32), denoted below as AL, which has a noncanonical Hamiltonian form

$$\dot{z} = P(z)\nabla H(z) \tag{41}$$

where $z = (p, q) = (p_1, \ldots, p_N, q_1, \ldots, q_N)$ and $p = u^*$, $q = u$ are the conjugate variables. The Hamiltonian is given by

$$H = \frac{\mathrm{i}}{h^3} \sum_{n=1}^{N} \left[h^2 p_n(q_{n-1} + q_{n+1}) - 2\ln(1 + h^2 q_n p_n) \right] \tag{42}$$

where the Poisson bracket tensor $P(z)$ is a $2N \times 2N$ skew-symmetric matrix

$$P(z) = \begin{pmatrix} 0 & -R \\ R & 0 \end{pmatrix} \qquad R = \mathrm{diag}[r_1, \ldots, r_N] \qquad r_n = \frac{1 + h^2 q_n p_n}{h} \tag{43}$$

so that the fundamental Poisson brackets are given in coordinates (p, q) by

$$\{p_m, q_n\} = -r_n \delta_{m,n} \qquad \{p_m, p_n\} = \{q_m, q_n\} = 0. \tag{44}$$

We need to construct discretizations of (41) preserving its essential Hamiltonian nature. If we denote the transformation from one timestep to the next by ψ, the appropriate quantity to preserve for higher-dimensional systems is given by

$$\psi'^T P \psi' = P \qquad \forall (p, q) \in \Omega \tag{45}$$

where ψ' is the Jacobian matrix of the transformation and P is the $2n \times 2n$-dimensional symplectic matrix defined by (43).

As mentioned above, equation (32) carries on its phase space a noncanonical symplectic structure and standard symplectic integrators are not immediately applicable. For example, implicit symplectic Runge–Kutta schemes for AL (41) do not exist. One approach to preserving the symplectic structure is to transform the system into a form for which standard symplectic integrators can be applied. In [30] two such transformations are studied. One transformation yields a noncanonical Hamiltonian system for which splitting methods can be applied. The second transformation, a Darboux transformation, reduces the AL symplectic structure to canonical form. This study indicates that the transformations introduce additional complexity into the form of the equations and that it is actually more efficient to integrate the AL system in its original noncanonical form [30].

For a general noncanonical Hamiltonian system, symplectic schemes can be constructed by noting that any transformation derived from a generating function is a symplectic map

Table 1. Maximum absolute error in the AL Hamiltonian obtained with S2 and R2 for $T = 500$.

N	4	4	16	16	32	32	64	64
t	1.0E−02	1.0E−03	1.0E−02	1.0E−03	1.0E−03	1.0E−04	5.0E−04	1.0E−04
S2	7.1E−06	7.1E−08	2.7E−04	2.7E−06	3.7E−06	5.1E−08	1.0E−06	1.0E−07
R2	1.3E−05	3.5E−08	2.2E−04	5.2E−07	6.0E−07	4.1E−09	1.2E−07	4.1E−09

(e.g. [29, 32]). In brief, using a truncation of the generating function, the following second-order symplectic scheme, which we denote by S2, is obtained for the AL system (see [30]):

$$\tilde{P}_n = \frac{(1 + h^2 q_n p_n) \exp\left(-hq_n \frac{\partial E}{\partial q_n}\right) - 1}{h^2 q_n} \qquad E = tG_1 + \frac{t^2}{2} G_2$$

$$\tilde{Q}_n = \frac{(1 + h^2 q_n \tilde{P}_n) \exp\left(h\tilde{P}_n \frac{\partial E}{\partial \tilde{P}_n}\right) - 1}{h^2 \tilde{P}_n} \tag{46}$$

where

$$G_1(\boldsymbol{P}, \boldsymbol{q}) = H \qquad G_2(\boldsymbol{P}, \boldsymbol{q}) = \sum_j \frac{1}{h}(1 + h^2 P_j q_j) \frac{\partial H}{\partial P_j} \frac{\partial H}{\partial q_j}.$$

As the scheme is implicit, to advance one timestep from $(\boldsymbol{p}, \boldsymbol{q})$ to $(\tilde{\boldsymbol{P}}, \tilde{\boldsymbol{Q}})$, system (46) is solved using a simple fixed-point iteration (FPI) procedure. The FPI converged rapidly for all values of t used in our numerical experiments.

In the experiments for the AL system we use initial data of the following form:

$$u(x, 0) = a(1 + 0.1 \cos(\mu x)) \tag{47}$$

with $a = 0.5$, $L = 2\sqrt{2}\pi$ and $\mu = 2\pi/L$. This initial data corresponds to one double point on the imaginary axis for the plane wave potential. Figures 9(*a*)–(*c*) show the error in the Hamiltonian obtained using S2 (46) and an explicit Runge–Kutta scheme, which we denote as R2 for (*a*) $N = 4$ with $t = 10^{-2}$, (*b*) $N = 16$ with $t = 10^{-2}$ and for (*c*) $N = 32$ with $t = 10^{-3}$. The symplectic scheme S2 preserves the Hamiltonian extremely well during long-time integrations as the error in the Hamiltonian oscillates in a bounded fashion and does not exhibit a linear drift as it does with R2. However, the linear error growth in H which occurs using the nonsymplectic method becomes less significant as the dimension of the system $2N$ increases and the timestep t decreases (compare figures 9(*a*)–(*c*)).

This behaviour is summarized in table 1 which provides the maximum error in H of the AL system as a function of N and t using schemes S2 and R2, i.e. for mesh sizes $N = 4$, 16, 32 and 64, each for two timesteps. The preservation of the second invariant I is not presented as it is qualitatively similar to H. The experiments with different timesteps t indicate that the error in the Hamiltonian is bounded by $\gamma_{S2} t^2$ for the method S2, whereas it behaves like $\alpha_{R2} t^2 + \beta_{R2} T t^3$ for the method R2. The dependence of the constants γ_{S2}, α_{R2}, and β_{R2} on the space discretization parameter h is less clear (see table 1).

Figure 9(*d*) shows the amplitude of q_1 of the solution obtained with the two integrators R2 and S2 using $N = 16$ and $t = 10^{-2}$. Solutions of the AL system exhibit regular quasi-periodic motion due to the fact that the AL flow occurs in general on an N-torus. For $t = 0.01$, a phase lag develops using R2 which becomes more pronounced as the system evolves. However, using $t = 0.001$ the solutions from the two integrators are virtually indistinguishable on the timescale examined. The amplitudes of the other lattice sites show similar qualitative behaviour.

With both schemes one must be cognizant of stability issues. This can be seen from the $N = 4$ and 16 cases. Keeping the timestep fixed and varying N (equivalently h), as h decreases the performance of both schemes degrades. This suggests that $t/h^2 < M$, for some
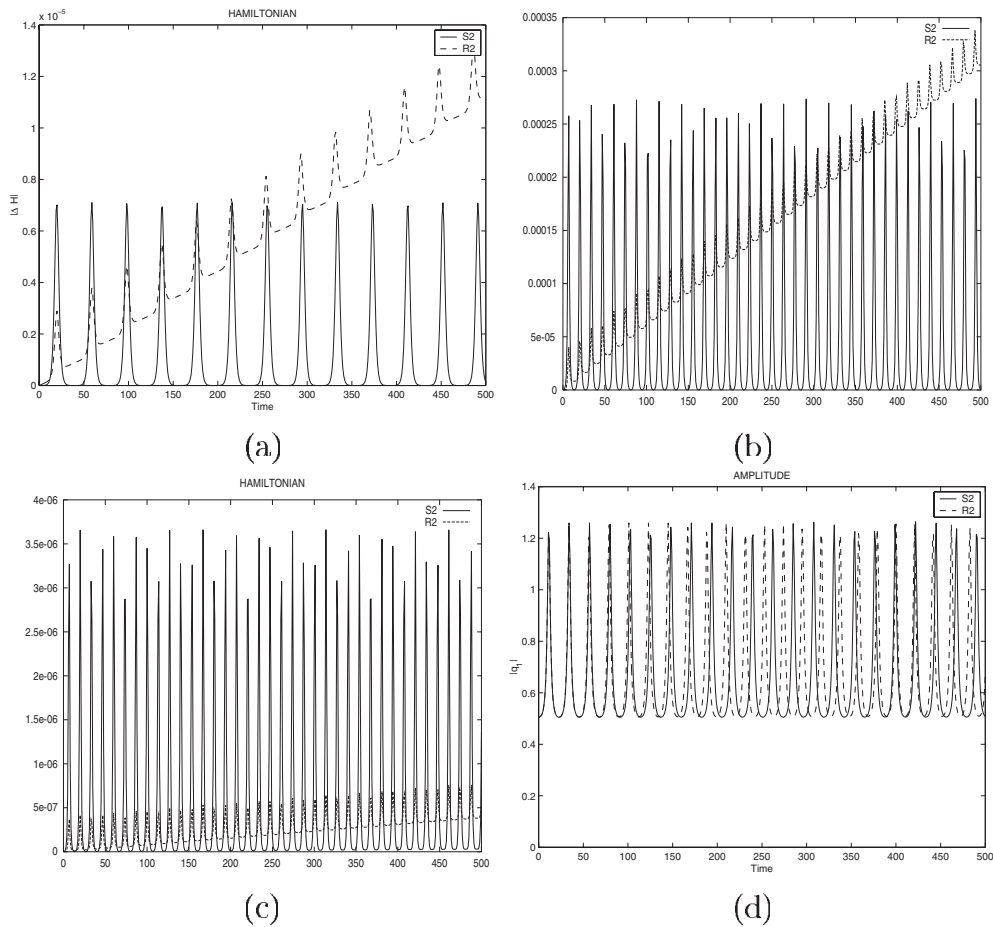
Figure 9. Comparison of integrators S2 and R2 for the noncanonical AL system: (*a*) error in the Hamiltonian for $N = 4$ with $t = 10^{-2}$, (*b*) error in the Hamiltonian for $N = 16$ with $t = 10^{-2}$, (*c*) error in the Hamiltonian for $N = 32$ with $t = 10^{-3}$, (*d*) amplitude of q_1 for $N = 16$ with $t = 10^{-2}$.

M, is required for stability. The instability is more pronounced for the explicit scheme R2 than for either of the symplectic schemes. It should be mentioned that R2, being an explicit scheme, is faster than S2 and the difference in computation time becomes more significant as the dimension $2N$ of the semi-discrete system is increased. At the same time the difference in accuracy of the two schemes manifests on a longer timescale, making $R2$ very attractive for intermediate integration times.

Next we examine the sG equation. As in the case of the NLS equation, the sG equation has an associated nonlinear spectrum which is invariant in time. The invariant spectrum corresponds to the action variables of the action-angle formulation of integrable finite-dimensional Hamiltonian systems and therefore provides a description of the qualitative properties of the flow. Numerical solutions destroy integrability in general which means that the spectrum, i.e. the action variables, are no longer time invariant. We will use preservation of the associated nonlinear spectrum as a basis for comparing the performance of symplectic and nonsymplectic schemes for the sG equation.

For the spatial discretization we use the exponentially accurate (for analytic solutions) Fourier pseudospectral method. Using the Hamiltonian function

$$H = \frac{1}{2} \sum_{n=-\frac{1}{2}N}^{\frac{1}{2}N-1} \left[|\dot{A}_n|^2 + \mu_n^2 |A_n|^2 \right] - \frac{1}{N} \sum_{j=-\frac{1}{2}N}^{\frac{1}{2}N-1} \cos\phi_j \tag{48}$$

where

$$A_n = F_n\{\phi\} := \frac{1}{N} \sum_{j=-\frac{1}{2}N}^{\frac{1}{2}N-1} \phi_j \exp(-2\pi \mathrm{i} n j/N)$$

and

$$\phi_j = F_n^{-1}\{A\} := \sum_{n=-\frac{1}{2}N}^{\frac{1}{2}N-1} A_n \exp(2\pi \mathrm{i} n j/N).$$

the Fourier pseudospectral discretization

$$\ddot{A}_n + \mu_n^2 A_n + F_n\{\sin\phi\} = 0 \tag{49}$$

is obtained from Hamilton's equations

$$\ddot{A}_j = -\frac{\partial H}{\partial A_j} \qquad \dot{A}_j = \frac{\partial H}{\partial \dot{A}_j}.$$

Thus, by discretizing the spatial variable, one reduces the infinite-dimensional sG system to a finite-dimensional canonical Hamiltonian system, written in the form

$$\frac{\mathrm{d}p_i}{\mathrm{d}t} = -\frac{\partial H}{\partial q_i} \qquad \frac{\mathrm{d}q_i}{\mathrm{d}t} = \frac{\partial H}{\partial p_i} \qquad i = 1, \dots, N \tag{50}$$

or more conveniently as

$$\frac{\mathrm{d}z}{\mathrm{d}t} = J^{-1}\mathbf{grad}H(z) \tag{51}$$

where $z := (p, q)^T$ and $J := \begin{pmatrix} 0_n & I_n \\ -I_n & 0_n \end{pmatrix}$ with 0_n and I_n denoting the zero and unit matrices of dimension n, respectively.

Without going into any details let us simply note that the resulting symplectic discretizations will be explicit since the Hamiltonian is separable

$$H(p, q) = T(p) + V(q).$$

This allows for very efficient explicit implementations using standard symplectic schemes.

For our numerical experiments, initial data of the following form is used,

$$u(x, 0) = \pi + 0.1\sqrt{1 - \mu^2} \cos(\mu x)$$
$$u_t(x, 0) = (0.1 \pm R)\sqrt{1 - \mu^2} \cos(\mu x)$$

with parameters $\mu = 2\pi/L$ and $L = 2\sqrt{2}\pi$. The spectra of these initial values for $R = 0$, $R < 0$ and $R > 0$ are shown in figure 10.

Note that this initial data is in the 'effectively' chaotic regime as the zeroth double point remains closed, i.e. the initial data is on the level set containing the homoclinic manifold. Closed double points cannot be preserved by the numerical schemes and in the following experiments one observes that the zeroth mode is immediately split into a gap state by the numerical scheme. Henceforth we choose $R = -0.1$, i.e. $u_t(x, 0) = 0$. Although we therefore
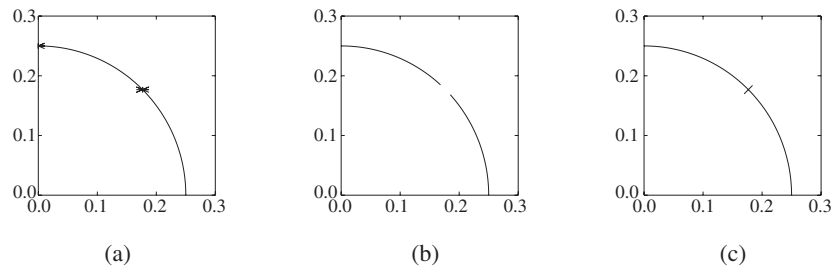
Figure 10. The nonlinear spectrum. (*a*) Homoclinic orbit. (*b*) Inside the homoclinic orbit. (*c*) Outside the homoclinic orbit.

only discuss initial values in an unstable regime, the conclusions are the same for initial values in stable regimes, see [10].

In order to measure the qualitative properties of the different symplectic and nonsymplectic discretizations, we monitor the time evolution of the spectrum. (Ideally it should remain invariant.)

To interpret the evolution of spectrum plots, note that under perturbations the complex double points can split in two ways: either into a gap along an arc of the circle or into a cross along the radius (cf figure 10). For each set of experiments, we compute a signed measure of the splitting distance for each complex double point as a function of time. Positive and negative values represent gap and cross states, respectively. Homoclinic crossings occur when the splitting distance passes through zero.

In order to ensure that the differences between the symplectic and nonsymplectic methods are due to the time discretization we use sufficiently many Fourier modes so that the Fourier spectral spatial discretization becomes essentially exact. We established numerically that $N = 32$ Fourier modes are sufficient. We have compared Runge–Kutta methods of different orders of accuracy, using *fixed* timesteps, with symplectic discretizations of the same order of accuracy. Although the deviation in the actions decrease with increasing order of accuracy, we have not found any appreciable difference between the symplectic and nonsymplectic discretizations, see [10]. Figures 11(*a*)–(*c*) are representative of our findings. Figures 11(*a*), (*b*) show a timeslice of $10\,000 \leqslant t \leqslant 10\,500$ for fourth-order Runge–Kutta (PS4RK) and symplectic (PS4SY) discretizations. For PS4RK the deviations in the action associated with the zeroth mode oscillates about 1.2×10^{-4} (figure 11(*a*)) whereas for PS4SY it oscillates about 5×10^{-5} (figure 11(*b*)). Further, the deviations in the action associated with the first mode are $\mathcal{O}(10^{-2})$ for all three schemes. Although the symplectic scheme does preserve the actions a little better there is no appreciable drift in the actions due to the Runge–Kutta integrator. However, the Runge–Kutta integrator can be made more efficient using variable timesteps. We apply the Runge–Kutta code, D02DDf, of the NAG library which is a fully adaptive timestepping method, to the pseudospectral method (PSNAG). Figure 11(*c*) shows that PSNAG does provide an improvement as it oscillates about 5×10^{-5}. The chaotic width (amplitude of the splitting distance) obtained with the fixed timestep has been diminished with this adaptive method. Consequently, for the long timescale regime, the slight advantage obtained with PS4SY has been eliminated using a variable timestep Runge–Kutta integrator. This is not surprising given the previous results obtained using S2 and R2 for the AL system. In that case the difference in accuracy of the two schemes is manifested on longer and longer timescales as the dimension of the system is increased.

In conclusion we emphasize that we are not concerned here with the computational efficiency of the numerical schemes; we wish to compare the ability of symplectic
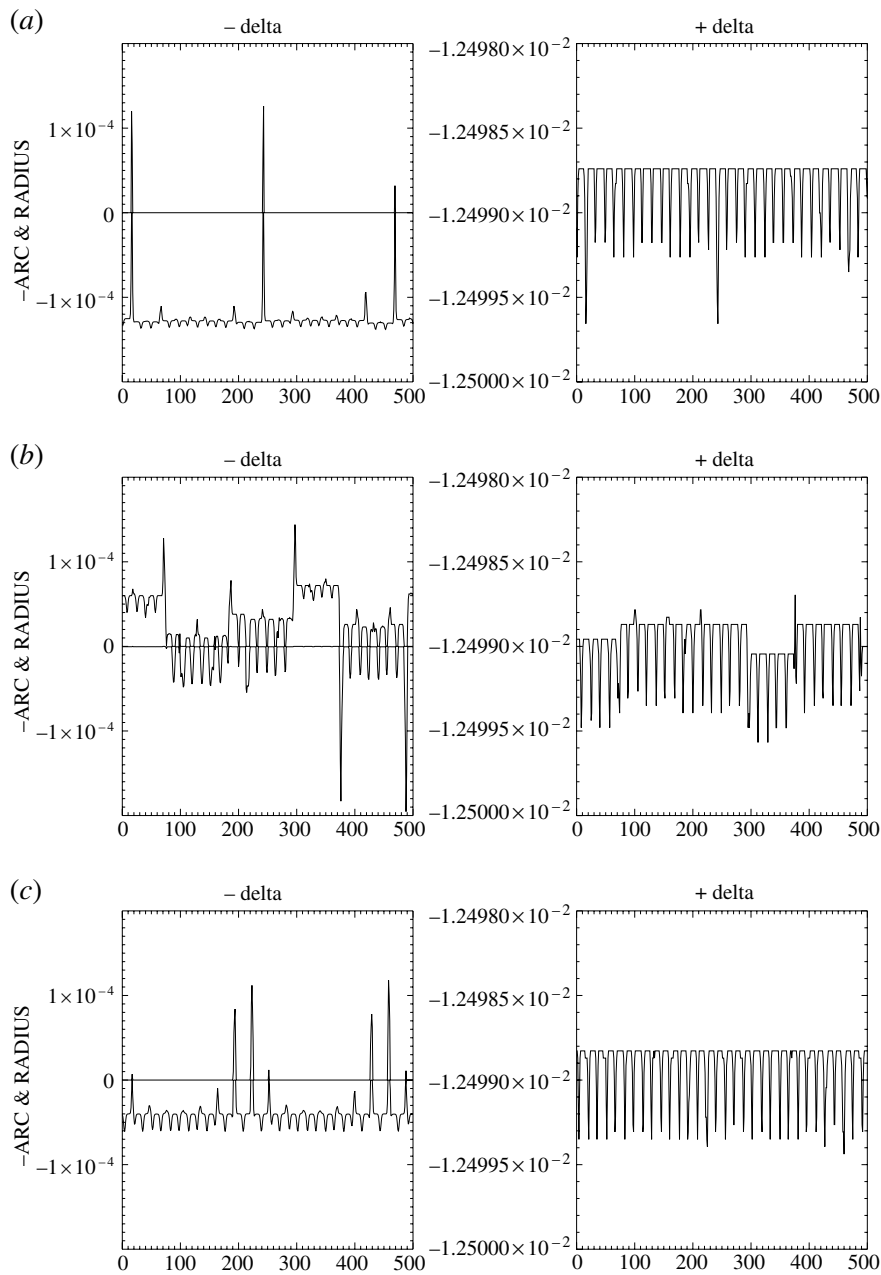
Figure 11. $u(x, 0) = \pi + 0.1 \cos \mu x$, $u_t(x, 0) = 0$, $N = 32$, $t = 10\,000$–$10\,500$. (a) PS4RK, (b) PS4SY, (c) PSNAG.

schemes to preserve the actions of integrable infinite-dimensional Hamiltonian systems with nonsymplectic schemes. Since we are only interested in symplectic properties, the specific method or implementation should not be important. In that sense our results are generally representative of symplectic schemes. Since our results fail to indicate significantly superior performance of symplectic schemes over (easily available) Runge–Kutta integrators for this

class of high-dimensional Hamiltonian systems (where it is possible to obtain an accurate measure of its qualitative properties) we believe that it is necessary for researchers to begin to be much more precise about the unique qualities and advantages of symplectic schemes.

Acknowledgments

References

[1] Ablowitz M J and Ladik J F 1976 Nonlinear differential-difference equations and Fourier analysis *J. Math. Phys.* **17** 1011–8

[2] Ablowitz M J and Segur H 1981 *Solitons and the Inverse Scattering Transform* (Philadelphia, PA: SIAM)

[3] Ablowitz M J and Clarkson P A 1991 *Solitons, Nonlinear Evolution Equations and Inverse Scattering* (Cambridge: Cambridge University Press)

[4] Ablowitz M J and Herbst B M 1989 On homoclinic boundaries in the nonlinear Schrödinger equation *Proc. CRM Workshop on Hamiltonian Systems, Transformation Groups and Spectral Transform Methods* ed J Harnad and J E Marsden (Montreal: CRM) pp 121–32

[5] Ablowitz M J and Herbst B M 1990 On homoclinic structure and numerically induced chaos for the nonlinear Schrödinger equation *SIAM J. Appl. Math.* **50** 339–51

[6] Ablowitz M J, Schober C M and Herbst B M 1993 Numerical chaos, roundoff errors and homoclinic manifolds *Phys. Rev. Lett.* **71** 2683–6

[7] Ablowitz M J and Schober C M 1994 Effective chaos in the nonlinear Schrödinger equation *Contemp. Math.* **172** 253–68

[8] Ablowitz M J, Herbst B M and Schober C M 1996 Computational chaos in the nonlinear Schrödinger equation without homoclinic crossings *Physica* A **228** 212–35

[9] Ablowitz M J, Herbst B M and Schober C M 1996 On the numerical solution of the sine-Gordon equation. I. Integrable discretizations and homoclinic manifolds *J. Comput. Phys.* **126** 299–314

[10] Ablowitz M J, Herbst B M and Schober C M 1997 On the numerical solution of the sine-Gordon equation. II. Performance of numerical schemes *J. Comput. Phys.* **131** 354–67

[11] Ablowitz M J, Hammack J, Henderson D and Schober C M 2001 Long-time dynamics of the modulational instability of deep water waves *Physica* D **152–3** 416–33

[12] Ablowitz M J and Schober C M 2001 Chaotic dynamics of modulational instability in optical fibres *Opt. Lett.* at press

[13] Bobenko A and Pinkall U 1994 Discrete surfaces with constant negative curvature *SFB 288 preprint* no 127

[14] McLaughlin D W, Bishop A R and Overman E A 1986 Coherence and chaos in the driven damped sine-Gordon equation: measurement of the soliton spectrum *Physica* D **19** 1–41

[15] McLaughlin D W, Bishop A R, Forest M G and Overman E A 1986 A quasi-periodic route to chaos in a near-integrable PDE *Physica* D **23** 293–328

[16] McLaughlin D W, Ercolani N and Forest M G 1986 Modulational instabilities of periodic sine-Gordon waves: a geometric analysis *Lect. Appl. Math.* **23** 149–66

[17] McLaughlin D W 1992 *Whiskered Tori for the NLS Equation. Solitons in the 80's* ed T Fokas and V Zakharov

[18] Ercolani N, Forest M G and McLaughlin D W 1990 Geometry of the modulational instability part iii: homoclinic orbits for the periodic sine-Gordon equation *Physica* D **43** 349–84

[19] McLaughlin D W and Overman E A 1994 Whiskered tori for integrable PDE's: chaotic behaviour in near integrable PDE's *Surv. Appl. Math.* **1** 83–200

[20] McLaughlin D W and Y Li 1994 Morse and Melnikov functions for NLS PDE's *Commun. Math. Phys.* **162** 175–214

[21] Forest M G and Lee J E 1986 Geometry and modulation theory for the periodic nonlinear Scrhödinger equation *Oscillation Theory, Computation and Methods of Compensated Compactness (IMA in Math and its Appl.)* vol 2 ed C Dafermos, J L Ercksen, D Kinderlehrer and M Slemrod (Berlin: Springer) pp 35–70

[22] McLaughlin D W, Cai D and Shatah J 1999 Spatial–temporal chaos and effective stochastic dynamics for a near integrable nonlinear system *Phys. Lett.* **253** 280–6

[23] McLaughlin D W and Cai D 2000 Chaotic and turbulent behaviour of unstable 1-D nonlinear dispersive waves *J. Math. Phys.* **41** 4125–53

[24] McLaughlin D W and Schober C M 1992 Chaotic and homoclinic behaviour for numerical discretizations of the nonlinear Schrödinger equation *Physica* D **57** 447–65

[25] Calini A, Ercolani N M, McLaughlin D W and Schober C M 1996 Mel'nikov analysis of numerically induced chaos in the nonlinear Schrödinger equation *Physica* D **89** 227–60

[26] Herbst B M and Ablowitz M J 1989 Numerically induced chaos in the nonlinear Schrödinger equation *Phys. Rev. Lett.* **62** 2065–8

[27] Hirota R 1977 Nonlinear partial difference equations III; discrete sine-Gordon equation *J. Phys. Soc. Japan* **43** 2079–86

[28] Molina M I and Tsironis G P 1993 Dynamics of self-trapping in the discrete nonlinear Schrödinger equation *Physica* D **65** 267–73

[29] Sanz-Serna J M and Calvo M P 1994 *Numerical Hamiltonian Problems* (London: Chapman and Hall)

[30] Islas A L, Karpeev D A and Schober C M 2001 Geometric integrators for the nonlinear Schrödinger equation *J. Comput. Phys.* **172** 1–33

[31] Schober C M 1999 Symplectic integrators for the Ablowitz–Ladik discrete nonlinear Schrödinger equation *Phys. Lett.* A **259** 140–51

[32] Channell P J and Scovel C 1990 Symplectic integration of Hamiltonian systems *Nonlinearity* **3** 1–13